

# Single-mode laser guiding in non-parabolic plasma channels for high-energy electron acceleration

Zsolt Léczi<sup>1\*</sup>, Szilárd Majorosi<sup>1</sup>, Nasr A. M. Hafz<sup>1,2</sup>

December 20, 2024

*1 ELI-ALPS, ELI-HU Non-Profit Ltd., Wolfgang Sandner utca 3., Szeged, H-6728, Hungary*  
*2 Doctoral School of Physics, Faculty of Science and Informatics, University of Szeged, 9 Dóm tér, H-6720 Szeged, Hungary*

\*Corresponding author: zsolt.leczi@eli-alps.hu

**Abstract** The discovery of laser wakefield acceleration in gaseous plasma was a major milestone that could lead to a significant reduction of size and cost of large electron accelerators. For higher-energy laser-driven electron acceleration guiding plasma channels were proposed, which are matched to the laser pulse parameters. For guiding a Gaussian beam, a parabolic density profile is needed, which is difficult to realize experimentally. The realistic channel profiles can be described by higher order polynomial functions which are not optimal for guiding due to the development of undesired distortions in the laser intensity envelope. However, here we show that for non-parabolic plasma channels well-defined matching conditions exist, which we call mode matching. This leads to the guiding of the fundamental mode only in the acceleration regime, where the plasma electron density is modulated by the high-intensity laser pulse. In this way we eliminate two deteriorating factors of laser wakefield acceleration, namely the mode dispersion and energy leakage. We apply this new matching condition for single-mode guiding in quasi-3D simulations to show that 10 GeV energies can be reached in a distance of less than 15 cm.

## 1 Introduction

High-energy RF-based (radio-frequency) particle accelerators delivering beams of charged particles have been of crucial importance in industry, science and technology for their applications, for example, in cancer therapy, material science, photon science and in discoveries of fundamental particles in nature [1, 2]. A good example for an operational large-size machine is the 3.4 km-long European X-ray Free Electron Laser (XFEL), which is driven by 17.5 GeV electron beams from a 1.7 km-long superconducting LINAC (linear accelerator). However, the cost of multi-km long accelerators is very high, especially, when the required particle energies are well-beyond one gigaelectronvolt (GeV) [3]. So, there is an important motivation for physicists and engineers to create alternative techniques to down-size particle accelerators in order to make them more affordable. Since the invention of the chirped-pulse-amplification technique [4], the laser pulses from table-top laser systems can be sufficiently intense to drive plasma wakefields [5] in gas (such as Hydrogen or Helium) targets that can be used to accelerate electrons to relativistic energies [6, 7] over extremely short distances. This is called laser wakefield acceleration (LWFA), a laser-based acceleration scheme involving CPA laser pulse as driver and underdense gaseous plasma medium. Laser wakefield accelerated GeV-class electron bunches by 100s of TW laser pulses have been demonstrated for more than a decade carrying 10s to 100s of pC total charge [8, 9, 10, 11, 12, 13]. The quality of these electron beams were sufficiently good for some applications, such as betatron X-ray radiation imaging and micro-CT (computerized tomography) of various objects [14]. On the other hand, there are continuous efforts to bring up the quality of the GeV beams from LWFAs to

meet more application requirements. It is also worth mentioning that there has been great efforts in the development of electron-beam driven plasma wakefield accelerators [15], but in that case the energy conversion efficiency is still too low.

LWFAs have shown a tremendous advancement [16, 17], thanks to the availability of commercial and in-house-built table-top terawatt and petawatt laser systems around the world [18, 19]. The ever-increasing laser peak power led scientists to approach the 10 GeV energy level within 20 cm acceleration distance [20, 21] in the plasma. Electron bunches with such high energy, which are naturally synchronized to the driving laser pulses, are important for revealing fundamental QED processes, such as the photon-recoil effect [22, 23], for linear colliders [24], and for driving XFEL-s.

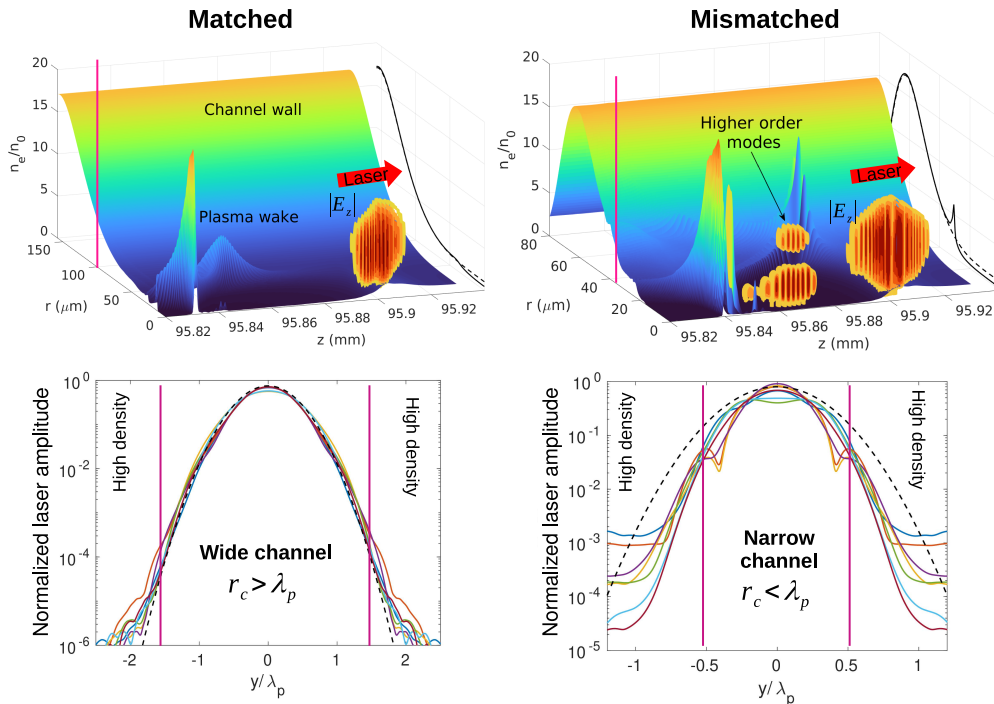


**Figure 1: Concept of the single-mode guiding for a relativistic-intensity Gaussian laser pulse:** We show the matched case on the *left* and the mismatched case is on the *right*. The figures in the top show the plasma density after  $\sim 10$  cm of propagation overlaid with the vertical cross-section of the linearly polarized laser pulse as orange-red colors. The longitudinal component of the laser field is used to represent the higher order modes and the main pulse with the same color code. On the bottom we show the  $z$ -averaged (within the full width at half maximum) absolute transverse field component at different time instances (solid curves) with the initial Gaussian-profile (dashed black curves) and we indicate the position at the channel radius ( $|y| = r_c$ ) with vertical lines. Here  $\lambda_p = 66\mu\text{m}$ . In the mismatched case the laser field contains higher order modes with significant amplitude that propagate behind the main pulse due to mode dispersion, while the laser pulse preserves its Gaussian-profile in the matched case.

Several methods have been developed to extend the acceleration length and to increase the electron energy. External guiding has been applied in the form of discharge capillary waveguides [8, 20, 21]. The most recent and most reliable channels are formed in elongated gas jets by means of hydrodynamic expansion followed by the optical field ionization of the gas medium, so-called HOFI channels [25, 26, 27], that can provide a meter-scale acceleration length [28] and operation at kilohertz repetition rate [29]. These plasma channels are highly flexible and can be easily matched to the laser focusing optics by tuning the delay time between the generating beam and main driver

pulse.

Even in the case of improved laser guiding the acceleration is limited by the pump energy depletion and electron dephasing [30]. In the case of low-density plasma channels, the latter is the critical negative effect that strongly limits the electron energy gain. By applying spatio-temporal shaping of the laser pulses, one can circumvent this limitation [31, 32, 33], but these advanced methods have not been tested with plasma channels yet. In the case of a guided laser pulse, another effect, which is the mode dispersion [34], can also ruin the acceleration efficiency. This is caused by the fact that the realistic channel density profile strongly deviates from the ideal parabolic shape, and higher-order Laguerre-Gaussian modes appear. In recent experiments, where the laser spot and channel entrance had similar diameters, these higher order modes were present in the channel [26, 35, 36], that caused strong envelope oscillation in the first several centimeters of the propagation.

In this work, we consider non-parabolic radial density profiles, very similar to those existing in hydrodynamic plasma channels [25, 26]. We propose the concept of a wide channel, where the channel diameter is much larger than the laser waist and it is larger than the plasma wavelength, allowing the propagation of the fundamental Gaussian laser mode only, thus the mode dispersion or mode beating effects can be almost completely eliminated. This regime of laser guiding relies on the self-generated channel density profile that is modulated by the laser's ponderomotive force. The idea is that, instead of using a parabolic channel density profile we consider a more realistic non-parabolic shape that is modulated by the laser pulse such that the plasma susceptibility, seen by laser pulse, acquires a parabolic shape. The self-modulated channel density and the increased relativistic mass of electrons establishes a condition which is ideal for stable single-mode propagation of an intense laser pulse in arbitrary channels. Our scheme is presented in Fig. 1, where two examples are shown: the left part corresponds to the ideal guiding (wide channel) and the right part present a non-ideal, mismatched case, where the laser envelope deviates significantly from the fundamental mode. In the case of matched guiding, the plasma wavelength is smaller than the channel radius, which is indicated by the vertical dashed lines in the lower pictures. We also show that the electron injection into the accelerating wake occurs more naturally in wide channels, whereas in narrow channels it is not always the case [35].

## 2 Results

### 2.1 Existence of mode matching at relativistic intensities

We consider a non-parabolic plasma channel, that is more realistic and comparable with density profiles obtained in HOPI channels used in recent experiments. See Eq. (7) in the Methods Section for a formula of a guiding plasma channel which is created by optical field ionization. In our study the channel radius is larger than the plasma wavelength:  $r_c > \lambda_p$ , where  $\lambda_p = 2\pi c/\omega_p$ ,  $\omega_p = (e^2 n_0/m_e \epsilon_0)^{1/2}$  and  $n_0$  is the density along the channel axis, at  $r = 0$ . One can realize this regime by using higher plasma density if the channel radius (or the waist radius of the channel forming beam) is fixed. From the standard theory of nonlinear wakefields [37] it is known that longitudinal density modulation enhances the spectral modulation of the laser pulse, which in turn enhances dephasing. In order to suppress this effect the laser field amplitude has to be small, or the laser waist must be smaller than the plasma wavelength [38]:  $w_0 < \lambda_p$ . These two conditions are the essence of the laser guiding preserving the initial (fundamental) transversal mode.

We apply the method of source-dependent expansion (SDE) [39] to analyze the laser beam evolution in a plasma channel with a radial density shape described by higher order polynomials. Since the laser intensity is sufficiently high for ponderomotive density modulation, we have to take into account the self-consistent electron density that is longitudinally averaged within the laser pulse. In this analysis the transversal density profile near the center of the laser pulse, caused by the ponderomotive pressure, can be well-described by the following function:

$$n_e(r) = n_0 F(r) = n_0 (f(r) - \delta n), \quad (1)$$

where  $f(r)$  is the unperturbed plasma channel profile (see Eq. (7)). The second term in the expression above is obtained by evaluating the Laplace operator on the locally averaged relativistic  $\gamma$  factor of electrons in the volume occupied by the laser pulse [40]:  $\delta n = 0.5k_p^{-2}\nabla_r^2\gamma$ , with  $\gamma = \sqrt{1 + a_0^2|E_L/E_0|^2/2}$ ,  $a_0 = eE_0/(m_e c\omega)$ ,  $E_0 = |E_L(0)|$ , where  $E_L$  is the complex radial envelope (see Methods section). The expression of transverse density modulation is derived for longer pulses, therefore throughout this work we use a factor of 0.5 in order to take into account the finite pulse duration. This numerical factor is close to the value that one can get after evaluating the integral in Eq. (119) in Ref. [43] or Eq. (9) in Ref [41]. considering a pulse length around one third of the plasma wavelength.

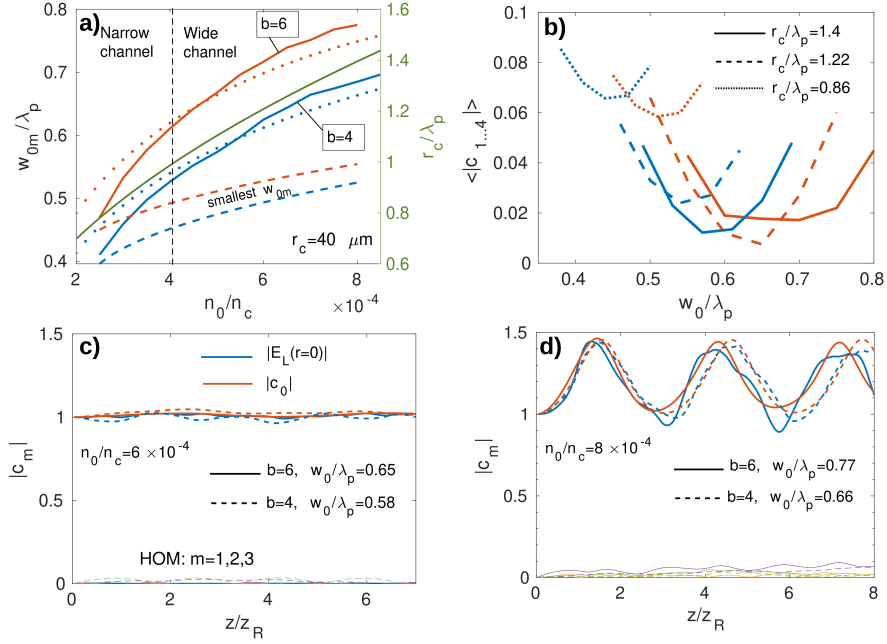


**Figure 2: Parameter-scan for high-order mode suppression:** (a) The upper limit of optimal waist radius (full lines) is shown for mode matching with  $a_0 = 2.7$  as a function of plasma density. There is an interval between the full and dashed lines, where mode-matching is possible. The dotted lines represent the laser waist numerically obtained from Eq. (6) with  $\kappa = 2.25$  and  $r^* = 1.5w_0$ . In (b) the sum of the average higher order modes are shown for different normalized channel radii (corresponding to different plasma densities). The absolute values of individual modes (normalized to  $a_0$ ) are shown in (c) and (d) for different density and  $w_0$  values, corresponding to perfect guiding (c) and mode matching (d). In the case of wide plasma channels ( $r_c > \lambda_p$ ) the laser spot, and peak laser field, strongly oscillates, while the laser beam practically consists of the fundamental mode only.

Using the SDE method we can monitor the evolution of higher order modes (HOM) within the laser beam as it propagates in the channel and we aim to minimize the amplitude of those modes. For this purpose an extensive parameter-scan has been performed where the laser field amplitude ( $a_0 = 2.7$ ) and channel radius ( $r_c = 40 \mu\text{m}$ ) were fixed and the initial laser waist radius is  $w_0 = \lambda_p$ . Then, for a given axial density value ( $2 \times 10^{-4} < n_0/n_c < 10^{-3}$ ) we look for the values of  $w_{0m}$ , where the amplitude of all high order modes is less than 10 % of the fundamental mode over many Rayleigh lengths. The resulting matched laser spot radii are shown in Fig. 2(a) for two channel wall parameters (b). One can see that a steeper channel wall permits mode-matching with wider laser spot and in a wide channel a broader interval of  $w_{0m}$  exist where the high-order modes are suppressed. These intervals are shown in Fig. 2(b) for different normalized channel radii (or different  $n_0$ ). From this analysis we see that mode matching is possible in narrow channels

as well, but the laser spot radius must be very small and the HOMs cannot be suppressed as effectively as in wide channel. The optimal parameters for perfect guiding is shown in Fig. 2(c), which corresponds to the double-matching case, where the laser spot and the fundamental mode amplitude, both stay constant. However, in reality the front and rear sides of the laser pulse witness different density modulation, which cannot be taken into account in the SDE model. This effect will prevent the laser pulse to be guided with constant spot size. One solution is called super-matching, which is presented in Ref. [42].

With slightly larger spot radius (in wide channel) periodic self-focusing and diffraction takes place without the development of higher order modes (see Fig. 2(d)), therefore mode-dispersion is greatly suppressed. In this case the whole laser pulse (front and rear sides) experiences a self-focusing condition and it oscillates more coherently, as a whole, as it is shown later by particle-in-cell simulations. This can be understood from the equation of spot size evolution:  $d^2w/dz^2 = (z_R^2 w^3)^{-1}(1 + \delta n/n_0 - P/P_c)$ , where  $z_R = \pi w_0^2/\lambda_0$  is the Rayleigh length,  $P$  is the laser power and  $P_c = k_p^2 a_0^2 w_0^2/32$  is the critical power. Inside the plasma cavity  $\delta n$  is negative, but in the first half of the laser pulse, or in the case of ultrashort pulses, it is positive [46], therefore  $P$  must be increased to achieve  $d^2w/dz^2 < 0$ , i.e. self-focusing. The dotted lines in Fig. 2(a) are given by the analytical expression derived in the next section, where the focusing strength of the channel is characterized by a free parameter ( $\kappa$ ). The discrepancy between the dotted and full lines in Fig. 2(a) originates from the constant value of  $\kappa$  used in the analytical expression Eq. (6). In principle  $\kappa$  is different for each physical setup which is treated self-consistently in the SDE method.

We note here that even in the most recent experiment [47] a narrow channel was used for high-energy electron acceleration:  $r_c/\lambda_p \approx 0.5$ ,  $w_0/\lambda_p = 0.5$ . Strong envelope oscillation and significant radial energy loss (leaky channel) was reported that is attributed to the presence of high-order radial modes. The suppression of those modes was achieved in a simulation where smaller spot radius was used:  $w_{0m} \approx 0.35\lambda_p$ . One can easily verify that this corresponds to the mode-matched case after extrapolating the full lines in Fig. 2(a), yielding  $w_{0m} \approx 0.3\lambda_p$  for  $r_c/\lambda_p \approx 0.5$ . This also confirms that mode-matching exists in narrow channels as well, but the amplitude of HOMs is always higher than in a wide channel.

## 2.2 Single-mode guiding of intense Gaussian laser pulses

In order to formulate a more precise condition for single-mode guiding we begin our analysis with the reduced wave equation of a monochromatic electric field  $E_x = \tilde{E}e^{-i\xi\omega/c}$ , with angular frequency  $\omega$ , using the comoving coordinate  $\xi = ct - z$  considering cylindrical symmetry:

$$\frac{1}{r} \frac{\partial}{\partial r} \left( r \frac{\partial \tilde{E}}{\partial r} \right) + 2i \frac{\omega}{c^2} \frac{\partial \tilde{E}}{\partial \tau} = \frac{\omega^2}{c^2} \chi(r) \tilde{E}, \quad (2)$$

where  $\tau = t = z/c$  and  $\tilde{E} = E_0 \exp(-r^2/w^2 - i\theta)$  is the complex envelope of a Gaussian beam that contains the information about the transverse phase profile (wavefront). We also introduce the relativistic plasma susceptibility expressed as

$$\frac{\omega^2}{c^2} \chi(r) = \frac{e^2}{\varepsilon_0 c^2 m_e} \frac{n_e(r)}{\gamma} = \frac{k_p^2}{\gamma} F(r), \quad (3)$$

where  $n_e(r) = n_0 F(r)$  is the radial profile of the plasma density seen by the laser pulse, and  $n_0$  is the electron density on the axis of the channel ( $r = 0$ ), which defines the value of the plasma wavenumber  $k_p$ . We also note here that the relation between  $\chi$  and the index of refraction ( $\eta$ ) is simply:  $\chi = 1 - \eta^2 = n_0/(n_c \gamma)$ , where  $n_c = \omega^2 m_e \varepsilon_0 / e^2$  is the critical density.

Inserting the formula of  $\tilde{E}$  in Eq. (2) and neglecting the variation in laser spot radius ( $dw/d\tau = 0$ ) leads to the evolution equation for the phase shift at the beginning of the interaction:

$$\frac{2\omega}{c^2} \frac{\partial \theta}{\partial \tau} = \frac{k_p^2}{\gamma} F(r) - \frac{4}{w^2} - \left( \frac{\partial \theta}{\partial r} \right)^2 - \frac{4r^2}{w^4}. \quad (4)$$

If  $\gamma = 1$  and  $\partial\theta/\partial r = 0$  initially, one can easily see that the phase shift will be constant in  $r$  with  $F = F_m = 1 + 4r^2/(k_p^2 w^4)$ , which is the condition for perfect guiding [43]. This leads to the conventional matching condition, where the parabolic channel radius is expressed as:  $r_c^2 = \epsilon k_p^2 w_0^4/4$  and  $f(r) = 1 + \epsilon r^2/r_c^2 = 1 + 4r^2/(k_p^2 w_0^4)$ . In general, in vacuum ( $F = 0$ ), the phase of a Gaussian laser beam is a parabolic function of radius,  $\theta = \theta(\tau, r^2)$ . It follows from Eq. (4), that in plasma  $\theta$  remains a purely parabolic function along the propagation if  $F(r)/\gamma = 1 + Cr^2$ , where  $C$  is constant in  $r$ , because  $\partial\theta/\partial r$  depends linearly on  $r$ . This ensures that the guided laser pulse preserves its initial Gaussian radial shape.

Therefore, the basic requirement to avoid the development of higher order modes is the existence of a parabolic electric susceptibility in the radial direction, i.e. perpendicular to the laser propagation direction. In the case of low intensity (non-relativistic) laser pulses this requirement is fulfilled by a parabolic density profile. However, in the case of linearly polarized high intensity pulses the plasma electron density is modified and for a purely Gaussian laser envelope  $\delta n$  can be evaluated analytically, thus the modified density profile is:

$$n_e(r) = n_0 F(r) = n_0 \left( f(r) - \frac{a_0^2 \exp(-2s^2)}{k_p^2 w_0^2 \sqrt{1 + (a_0^2/2) \exp(-2s^2)}} \right), \quad (5)$$

where  $s = \sqrt{2}r/w_0$ . From this equation it follows that in order to avoid full blow-out regime ( $n_e(0) > 0$ ) the spot size should satisfy  $k_p w_0 > a_0/(1 + a_0^2/2)^{1/4}$ , meaning that  $w_0 > \lambda_p/3$  for  $a_0 < 4$ , which holds in our parameter-space. One can easily verify that close to the axis  $\delta n$ , used in Eq. (5), well reproduces the density modulation used in the linear regime for  $a_0 \ll 1$ , which is [42, 43]:  $\delta n^{lin} = (a_0^2/4)k_p^{-2}\nabla_r^2[\exp(-s^2)]$ . Following the requirement of wide plasma channel, our analysis is restricted to the situation when  $w_0 < r_c$ , which means that the channel density profile can be described by a polynomial function alone in the vicinity of the laser pulse,  $f(r) \approx 1 + \epsilon(r/r_c)^b$ .

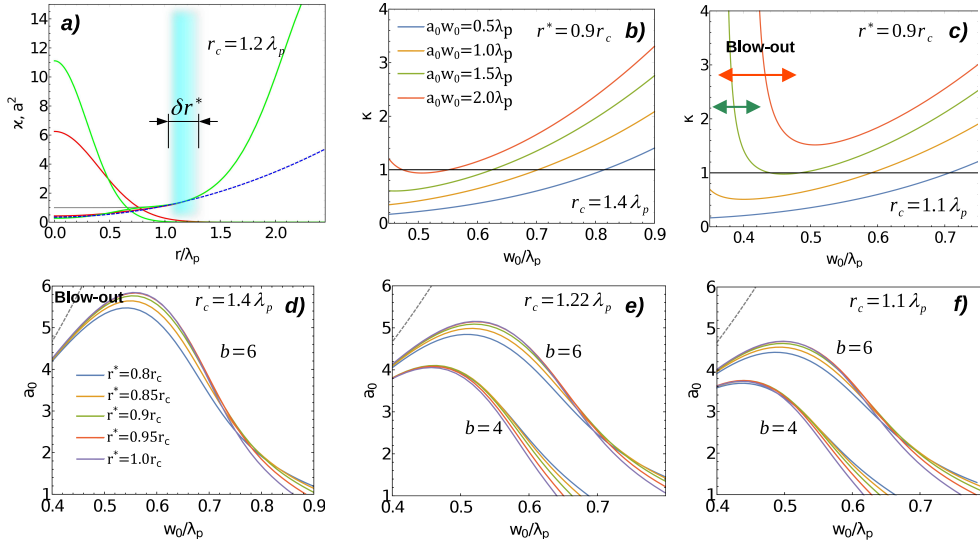


Figure 3: **Parameters for single-mode guiding:** (a) Conceptual description of susceptibility matching for a given initial plasma channel density profile ( $b = 6$ ) with two laser envelopes having the same power (green and red). The generated quasi-parabolic guiding structure is also shown by the same colors, which are very similar to a parabolic function (blue dashed line) for  $r < r_c$ . In (b,c) the focusing parameter ( $\kappa$ ) is shown for  $r^* = 0.9r_c$  and for constant laser powers indicated by the colors. In (d,e,f) the effect of  $r^*$  is analysed in the mode-matching condition for  $\kappa = 2$ . The gray dashed line shows the lower boundary of the blow-out regime.

One can recognize that in Eq. (2) the radial coordinates can be normalized with  $k_p$  (using

the identity Eq. (3)), thus from now on,  $\chi = n_e/(n_c\gamma)$  is replaced by  $\omega_p^2/\omega^2\chi = n_e/(n_0\gamma)$ . We can denote  $\chi = F/\gamma = n_e(r)/(n_0\gamma(r))$  as the modified and  $\chi_{opt} = \chi_0 + 4\kappa r^2/(k_p w_0^2)^2$  as the ideal susceptibility profile in the plasma channel for optimal guiding. Here  $\chi_0 = n_e(0)/(n_0\gamma_0)$ , with  $\gamma_0 = \gamma(r=0)$ , and  $\kappa$  is a free parameter, that expresses the focusing strength of the modified plasma channel. For  $\kappa = 1$  the laser would be guided without a change in the transversal envelope. Actually, in Fig. 2(c) such guiding is observable, but  $\kappa$  can have larger values as well without generating high order radial modes (see Fig. 2(d)). For a realistic laser pulse (finite duration)  $\kappa = 1$  cannot be satisfied along the whole pulse, therefore we use oversized laser spots, which yields  $\kappa > 1$  in each longitudinal slice of the laser pulse.

Next, we look for the laser parameters that generate a modified susceptibility profile (Eq. (5) divided with  $\gamma$ ) which closely resembles a parabolic function in the radial interval  $0 < r < 2w_0$ . In Fig. 3(a) it is shown that in the case of a wide channel ( $r_c > \lambda_p$ ) within the laser waist radius ( $r < w_0$ ) everything is quasi-parabolic. At larger radial position the plasma density is not modified and it is described by  $f(r)$ . The problem of finding the matching condition is reduced to a fitting problem where the parabolic shape has to be joined with the initial profile at a position  $r^*$ . From Fig. 3(a) it is apparent that  $r^*$  can take values from a limited interval around  $r_c$ . In the case of narrow channels the ponderomotive density modulation depends much stronger on  $w_0$  and reliable fitting is not possible. Another reason is that in narrow channel the density modulation is larger, which can be seen by comparing the black curves in the vertical planes in the upper pictures of Fig. 1.

We impose the fitting criteria  $\chi(r^*) = \chi_{opt}(r^*)$  to acquire a relation between the free parameters of the system. By enforcing  $\chi$  to be equal to the theoretically optimal shape (parabolic) at  $r = r^* > w_0$  we find the laser parameters needed for the creation of a self-generated parabolic  $\chi$ . This equality leads to an analytical expression for the characteristic channel radius:

$$r_c = r^* \left[ \frac{G_1}{\epsilon} \left( \frac{1 - a_0^2/(\gamma_0 w_0^2 k_p^2)}{\gamma_0} + \frac{a_0^2 \exp(-2s^{*2})}{G_1 G_2 w_0^2 k_p^2} + \frac{2s^{*2} \kappa}{k_p^2 w_0^2} \left( 1 - \frac{a_0^2}{\gamma_0 w_0^2 k_p^2} \right) - \frac{1}{G_1} \right) \right]^{-1/b}, \quad (6)$$

where  $s^* = \sqrt{2}r^*/w_0$ ,  $\gamma_0 = \gamma(r=0)$ ,  $G_1 = \sqrt{1 + (a_0^2/2) \exp(-s^{*2})}$  and  $G_2 = \sqrt{1 + (a_0^2/2) \exp(-2s^{*2})}$ . In this expression the values  $\epsilon$  and  $b$  can be taken from Table 1. Now Eq. (6) represents a new matching condition that ensures a clean propagation of the fundamental mode only, and it is different from the matching condition used to suppress the envelope oscillation in a parabolic channel, well-known in the literature [43]. At this point three parameters remain unknown, the focusing strength ( $\kappa$ ), the laser spot ( $w_0$ ) and peak intensity ( $a_0$ ). They can be related by fixing the value of  $r_c$  in Eq (6), as we did in Fig. 2(a), but the parameter  $r^*$  is still unknown. However, from Fig. 3 it is seen that  $r^*$  should be close to  $r_c$  and for qualitative explanation of Fig. 2(a,b) we can choose  $r^* = 0.9r_c$ . Doing so,  $\kappa$  can be expressed from Eq. (6) to present its dependence on the laser parameters. This is done in Fig. 3(b,c) in the wide channel regime for constant laser power. Taking any point on those curves where  $\kappa > 1$  will result in a mode-matched propagation with initial self-focusing and periodic envelope oscillation, as it is shown in Fig. 2(d). During self-focusing the laser spot decreases, according to the curves in Fig. 3(b,c), down to the point where  $\kappa < 1$  and diffraction becomes dominant, thus  $w$  increases again. This explains the resistance of a wide channel against the development of HOMs, even if the envelope strongly oscillates. In a narrower channel we may enter the blow-out regime (see Fig. 3(c)), if the initial  $a_0$  is too large, while the range of possible initial parameters is smaller (see also Fig. 2(b)).

Although the value of  $r^*$  was chosen arbitrarily, in Fig. 3(d,e,f) it is shown that it does not influence the mode matching condition, where  $\kappa = 2$ . We have verified that the effect of  $r^*$  on the shape of the mode-matching curves is significant only when  $w_0$  approaches the value of  $r_c$ . Using Eq. (6) with  $r^* \approx 0.9r_c$  it is possible to find the matched laser parameters for an arbitrary channel if  $w_0$  is large enough to avoid blow-out ( $2 < \kappa < 3$ ) and  $w_0 < \lambda_p < r_c$ .

The example shown in Fig. 1 corresponds to the matched case shown in Fig. 3(e) for  $b = 4$ ,  $w_0 = 0.6\lambda_p$ ,  $a_0 = 2.4$ ,  $\kappa = 2$ . We further illustrate the importance of guiding in a wide channel in Fig. 4, where two simulations are shown with exactly the same laser pulse, but the channel

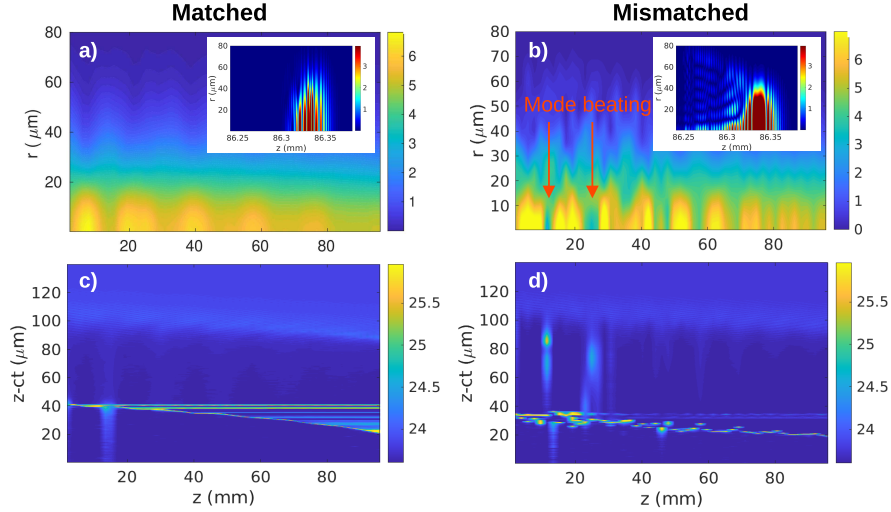


Figure 4: **Comparison between matched and mismatched guiding:** (a) and (b) shows the evolution of the radial profile of the axially averaged laser field amplitude (in units of TV/m). The insets show the cross-section of the laser pulse near the end of the channel. Strong mode dispersion in the mismatched case is clearly visible. In (c) and (d) the axial lineouts of the wake density in the first bubble are shown on logarithmic scale.

parameters are different. The laser parameters are  $w_0 = 0.7\lambda_p = 40 \mu\text{m}$ ,  $a_0 = 2.5$  and it has 22 J energy. In the matched case the channel radius is calculated using Eq. (6) and it is  $r_c = 1.43\lambda_p = 82 \mu\text{m}$  with  $n_0 = 3.45 \times 10^{17} \text{ cm}^{-3}$ , while in the mismatched case  $r_c = w_0 = 0.54\lambda_p = 40 \mu\text{m}$  with  $n_0 = 2 \times 10^{17} \text{ cm}^{-3}$ . In the matched case very smooth and regular envelope oscillation is observed, while in the mismatched case strong mode beating takes place, when the laser intensity maximum is not on the axis. This has a significant influence on the wakefield formation, shown in Fig 4(d). The spectra of generated electron bunches are shown in Fig. 7 (for 22 J pulse energy).

### 2.3 Periodic injection of plasma electrons into an oscillating bubble

An intrinsic property of the proposed wide plasma channels is that the self-generated parabolic profile leads to self-focusing ( $\kappa > 1$ ), because the radial steepness of the refractive index is larger than the one required for perfect guiding. This can result in self-injection of the electrons when certain conditions are met. This mechanism is similar to the wave-breaking, when the velocity of some electrons participating in the wave becomes larger than the peak velocity of the wave itself. The electrons are injected each time the laser pulse gets focused, which is seen in Fig. 5(a) and (b). There is a correlation between the evolution of the laser envelope and the spectrum of the injected electrons. The parameters of the presented simulation are:  $n_0 = 2.5 \cdot 10^{17} \text{ cm}^{-3}$ ,  $r_c = 1.43\lambda_p$ ,  $a_0 = 2.6$ ,  $w_0 = 0.72\lambda_p$ ,  $b = 4$ ,  $\epsilon = 1.5$  and the intensity envelope FWHM duration is  $t_L = 0.3\lambda_p/c = 69 \text{ fs}$ . The envelope oscillation is damped due to broadening of the laser frequency spectrum, or red-shifting [49]. Different wavelengths oscillate with different periodicity and they have different phase velocity, which leads to an overall smoothing of the oscillation [43].

The variation in the laser peak intensity is imprinted in the evolution of the cavity length, that is shown in Fig. 5(c). The effect of self-phase modulation [44, 45] is clearly visible in the density modulation near the position of the laser pulse (indicated by the white arrow), which gets sharper due to the self-compression. However, this effect appears only at the end of the acceleration. At the beginning of the propagation the oscillation of the bubble leads to a few microns variation in the position of the bubble's peak density in a time window of  $(10 \text{ mm})/c \approx 30 \text{ ps}$ , which results in  $\sim 10^{-4}c$  oscillation amplitude of the bubble's phase velocity ( $v_p$ ). This variation of the phase velocity leads to the self-injection of the electrons accumulated in the back of the bubble, where



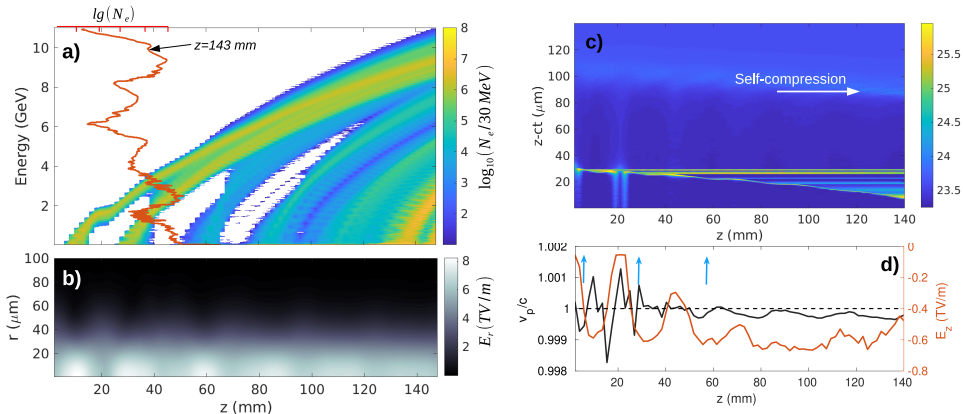


Figure 5: **Temporal evolution of the acceleration:** (a) Electron energy spectrum along the propagation distance. In (b) the axially averaged laser field modulus is shown, where the periodic focusing and defocusing of the laser pulse along the plasma channel is clearly visible. Each focusing triggers an injection event. The history of the axial density profile ( $\log_{10}[n_e]$  with units of  $m^{-3}$ ) of the nonlinear wakefield is shown in (c), where the horizontal stripes correspond to the injected electron bunches moving with nearly the speed of light. (d) The peak electric field in the back of the bubble is shown by the red line, while the velocity of the node of the wave (phase velocity of the plasma wave) is shown by the black line. As indicated by the blue arrows, self-injection occurs, when the electric field is strong enough and the phase velocity is sufficiently low.

they experience  $\sim 0.1$  TV/m accelerating field. In a distance of 1 mm some part of the electrons can easily gain  $> 100$  MeV energy, corresponding to a Lorentz factor  $\gamma_e > 200$ , that is much larger than the Lorentz factor associated with the phase velocity  $\gamma_p = (1 - v_p^2/c^2)^{-1/2} \approx 100$ . As we show in the following, the oscillating phase velocity leads to an oscillation in the space charge field near the back of the bubble, which is the main reason for self-injection to occur.

One can understand the process of self-injection by taking a closer look at the kinematics of a single electron moving in an evolving bubble. From Fig 6(a) it is clear that electrons originating from a region close to the axis ( $r = 0$ ) can be injected (red trajectories). Electrons being farther away from the axis experience a transverse ponderomotive force, due to the Gaussian laser envelope, and contribute to the formation of the wake structure. By looking at the velocity components of these electrons (in Fig. 6(b)) one can see that their maximum velocity does not approach the speed of light, but it is large enough to spend some time in the back of the bubble where the high density shell is formed. The highest density is reached on the axis (density peak), where the electrons have the highest velocity (close to the speed of light) and they can contribute for a longer time to the charge accumulated in this region, which is practically co-moving with the laser. The charge accumulation is clearly visible in Fig. 6(d), and it is evident that electrons can spend more time in the density peak when the phase velocity of the wake is less than the speed of light (see the black curve in Fig. 6(d)). The charge in the back of the bubble is calculated by summing up all electrons that are in the vicinity of the density peak, within  $4 \mu\text{m}$  distance. When the accumulated charge and the accelerating field are high enough (at the position  $\approx 7$  mm in Fig. 6(c)) the electrons can acquire a velocity that is large enough for wave-breaking (red curve in Fig. 6(d)). This mechanism is called longitudinal self-injection [48].

### 3 Discussion

The concept of wide plasma channel was tested for different laser energies and geometrical parameters, that are summarized in Fig. 7(a). These results suggest that the maximum electron energy can be well above 10 GeV using a PW-class laser pulse and a 14 cm long channel. An interesting

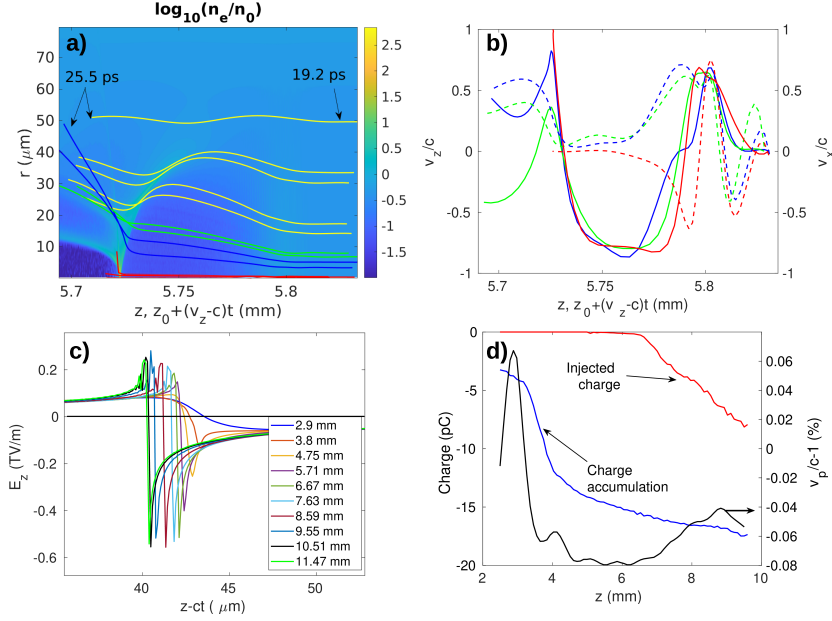


Figure 6: **Details of longitudinal self-injection:** (a) Electron density distribution overlaid with several electron trajectories originating from different radial positions. Here  $z_0$  is the initial position of the tracked electrons and  $v_z$  is their longitudinal velocity. Some of them, which are close to the propagation axis, can be injected (red curves). (b) Velocity phase-space evolution of selected electrons from different region of the plasma. The colors correspond to the electrons shown by the same colors in (a). The right vertical axis shows the transversal velocity (dashed lines). The red trajectory corresponds to an electron which gets injected. (c) Temporal evolution of the axial accelerating field in the moving frame. (d) Evolution of the charge in the back of the bubble (blue) and of the injected charge (red). The black curve (right axis) shows the phase velocity of the density peak.

fact is that even after this significant energy gain the laser pulse still contains 70 % of its initial energy, therefore in the case of the blue curve in Fig. 7(a) a short high-density gas jet can be placed after the 14 cm long channel to boost the electron energy even more. It is also seen that a mismatched laser pulse generates smaller cut-off energy and much lower injected charge compared to the mode-matched case. The mismatched case (green curve in Fig. 7(a)) corresponds to the LWFA in a narrow channel, which was realized experimentally [26], where no self-injection was observed, electrons were accelerated when ionization injection was used [36]. The fact that in our simulation we observe self injection is attributed to the steepness of the channel density, which was  $b = 4$  in this case. With  $b = 6$  we did not observe self-injection in this mismatched case. The irregular envelope oscillation (see Fig. 4) caused by the presence of higher order modes prohibits the charge accumulation, shown in Fig. 6(d), thus the probability of electron self-injection is much smaller.

The immediate consequence of longitudinal self-injection is the low transverse emittance of the accelerated electron bunch. From Fig. 6(a),(b) it is clear that the injected electrons have a very small transverse momentum and a micrometer-scale transverse displacement which leads to small divergence and source size, which is shown in Fig. 7(b). The mismatched case is not shown here, because we considered electrons with higher than 5 GeV.

The robustness of the wide channel LWFA was further tested with 15 J pulse energy as well, which was used in experiments [26]. For  $a_0 \approx 2.5$  the required laser spot size is around  $w_0 = 34 \mu\text{m}$  and the matched plasma density and channel radius are  $5 \times 10^{17} \text{cm}^{-3}$  and  $r_c = 60 \mu\text{m}$ , respectively. The simulation showed that, similarly to the experiment, 5 GeV electron cut-off energy is reached, but the acceleration distance was only 7 cm, i. e. 3 times shorter than that used in the experiment.

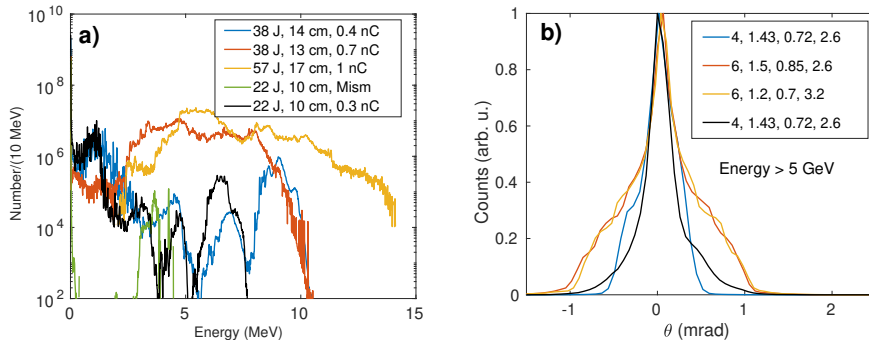


Figure 7: **Electron beam properties for different laser and plasma parameters:** (a) Energy spectra for different laser energies and channel lengths. (b) The corresponding divergence angle of electrons in the plane of laser polarization ( $\theta = \arctan(p_x/p_z)$ ). The numbers in the legend represent the following parameters:  $b, r_c/\lambda_p, w_0/\lambda_p, a_0$ . The focusing strength is  $k = 2$  in the case of the yellow curve, in other cases it is  $\kappa = 2.5$ .

We also note, that in our case self-injection dominates, but choosing slightly smaller  $\kappa$  (smaller  $a_0$ ) self-injection can be avoided and Nitrogen dopant can be used to trigger electron injection at the very beginning of the channel, which would lead to higher cut-off energy.

Finally, we can compare the laser waist radius, used in a wide channel, to the one required for self-guiding, which is given by  $w_0 = \sqrt{\gamma}\lambda_p/\pi$ . For  $a_0 = 2.5$  one obtains  $w_0 = 0.45\lambda_p$  that is much smaller than the matched spot size in our simulations. It means that a given plasma density in a wide channel supports acceleration driven by a larger pulse energy (larger spot size). The energy gain presented here fits well, and even surpasses, the theoretical prediction of the dephasing-limited LWFA (Eq. 6 in Ref. [50]), while in recent experiments the maximum energy barely reaches [21], or it is lower than the theoretical estimate [26, 36]. If we consider the mentioned energy scaling and 2 PW laser power, it will be possible to reach 40 GeV electron energy with an axial plasma density of  $3.3 \times 10^{16} \text{ cm}^{-3}$  and with a laser spot radius of  $120 \mu\text{m}$ . In this case the required laser pulse energy is 200 J (pulse duration is 100 fs) and the acceleration distance is slightly longer than 1 meter [28], that scales with the Rayleigh length (or with square of the laser spot size). This energy is already very close to the maximum electron energy ever produced in linear accelerators [51].

## Methods

### Main parameters of a HOFI plasma channel

The radial density profile in discharge and hydrodynamic plasma channels are commonly described by a polynomial function, which is multiplied by a Super-Gaussian in order to mimic the density modulation inside the radially expanding hydrodynamic shock:

$$n_e = n_0(1 + \epsilon\rho^b) \exp(-\beta\rho^p), \quad (7)$$

where  $\rho = r/r_c$ ,  $\beta \ll 1$ ,  $p \gg 1$  and  $b$  is a positive number characterizing the channel density profile. The characteristic radius of the channel is  $r_c$ . The parameter  $\beta$  is easily expressed as function of the other parameters by defining the maximum density in the channel wall  $n_e(\rho_m) = n_{max}$ , where typically  $n_{max} \sim 20n_0$  and  $\rho_m \approx 2$  is the position of the maximum density. The value of  $\rho_m$  can be varied and it directly depends on the channels' expansion time (or on the delay of the main pulse). The values  $\epsilon$  and  $b$  can be related by the requirement  $dn_e(\rho_m)/dr = 0$ , leading to the equation:

$$\beta p \rho_m^{p-1} (1 + \epsilon \rho_m^b) = \epsilon b \rho_m^{b-1}, \quad (8)$$

where  $\beta = -(1/\rho_m^p) \ln[(n_{max}/n_0)/(1 + \epsilon\rho_m^b)]$ . This equation is solved numerically to obtain the set of parameters that are used in our analysis presented in the main text. In the Table below  $n_{max} = 16n_0$ .

|      |                | <b>b</b>                     | <b>2</b> | <b>3</b> | <b>4</b> | <b>5</b> | <b>6</b> | <b>7</b> |
|------|----------------|------------------------------|----------|----------|----------|----------|----------|----------|
| p=8  | $\rho_m = 1.8$ | <b><math>\epsilon</math></b> | 5.9      | 3.75     | 2.36     | 1.5      | 0.94     | 0.6      |
|      | $\rho_m = 2$   |                              | 4.8      | 2.7      | 1.55     | 0.88     | 0.5      | 0.28     |
|      | $\rho_m = 2.2$ |                              | 4        | 2        | 1        | 0.55     | 0.28     | 0.14     |
| p=10 | $\rho_m = 1.8$ | <b><math>\epsilon</math></b> | 5.66     | 3.5      | 2.1      | 1.3      | 0.8      | 0.5      |
|      | $\rho_m = 2$   |                              | 4.58     | 2.5      | 1.4      | 0.77     | 0.43     | 0.23     |
|      | $\rho_m = 2.2$ |                              | 3.8      | 1.9      | 0.96     | 0.48     | 0.24     | 0.12     |

Table 1: Parameters of the plasma channel: Values of  $\epsilon$  (channel wall steepness) for different  $p$ ,  $b$  and  $\rho_m$  parameters. The red numbers are the values used in or simulations.

### Source-dependent expansion method for analysis of radial mode evolution

Here we recall the main equations of the source-dependent expansion method, developed in Ref. [39], with the assumption of full rotational symmetry, meaning that the higher-order azimuthal modes are neglected. For the modeling of the spatial (or temporal) evolution of the laser envelope we consider the reduced wave equation, Eq. 2:

$$\nabla_{\perp}^2 E_L + 2ik\partial E_L/\partial z = S = k^2[n_e/(\gamma n_c)]E_L = k^2\chi E_L, \quad (9)$$

where the higher order longitudinal derivatives are neglected which corresponds to the slowly varying envelope approximation. The next step is to express the solution of Eq. (9) as a combination of Laguerre-Gaussian modes:

$$\frac{E_L}{E_0} = \sum_{m=0}^M c_m D_m = \sum_{m=0}^M c_m L_m^0(2r^2/w^2) \exp[-(1-i\alpha)r^2/w^2], \quad (10)$$

where  $\alpha$  is related to the wavefront curvature and  $c_m$  are the mode coefficients, which are complex numbers containing information about the phase shifts and they are proportional to  $w_0/w$ . In the case of the fundamental mode, in vacuum,  $\alpha = z/z_R$ , where  $z_R = \pi w_0^2/\lambda$  is the Rayleigh length and  $w = w_0 \sqrt{1 + (z/z_R)^2}$ , which are used as initial conditions in the presented model, assuming that the focus position is at  $z = 0$ . By substituting Eq. (10) into Eq. (9) it is possible to derive a simple equation for the evolution of the mode coefficients [39]:

$$\partial c_m / \partial z + A_m c_m - im B c_{m-1} - i(m+1) B^* c_{m+1} = -i F_m, \quad (11)$$

where  $B = F_1/c_0$ , and the superscript  $*$  refers to the complex conjugate and  $A_m$  has the form:

$$A_m(z) = 2\alpha/(kw^2) - (B)_i + i(2m+1)[2/(kw^2) + (B)_r], \quad (12)$$

where the subscripts refer to the real ( $(\cdot)_r$ ) and imaginary ( $(\cdot)_i$ ) part of the quantity.

The function  $F_m(z)$  represents a coupling term between the neighboring radial modes and it is calculated using the source term:

$$F_m(z) = \frac{2}{k} \int_0^\infty (r/w^2) S D_m^* dr. \quad (13)$$

Finally the evolving parameters  $\alpha, w$  are calculated with the following equations:

$$w' = 2\alpha/(kw) - (B)_i w, \quad (14)$$

$$\alpha' = 2(1 + \alpha^2)/(kw^2) + 2[(B)_r - (B)_i \alpha], \quad (15)$$

Equations (11 - 15) can be used to calculate the beam profile at any position  $z$  using Eq. (10) with the assumption that  $m = 0$  is the strongest mode and  $c_0$  is the largest amplitude in the field composition. This condition holds in the case of close-to-matched beam profiles, which we consider in our work.

## Particle-in-cell simulations

For the numerical modeling we use FBPIC [52], a quasi-3D simulation code, with the moving window feature. The velocity of the window is exactly the speed of light in vacuum. The simulation domain is represented by  $3000 \times 800$  grid points, with grid spacing of 40 nm and 200 nm in the longitudinal and transverse dimensions, respectively. Two azimuthal modes are used and the number of macro-particles per cell is 64 ( $N_z \times N_r \times N_\theta = 2 \times 4 \times 8$ ). We assume pre-ionized gas and the ions are immobile, forming a neutralizing positive background. The radial plasma density profile is given by Eq. (7). The laser pulse has Gaussian temporal and spatial envelope, and it is focused at the entrance of the plasma channel.

### Acknowledgement

We acknowledge KIFÜ/NIIF for awarding us access to the Komondor HPC located in Debrecen, Hungary. The ELI-ALPS project (GINOP-2.3.6-15-2015-00001) is supported by the European Union and co-financed by the European Regional Development Fund.

**Data availability statement** The data that support the findings of this study are available from the corresponding author upon reasonable request.

## References

- [1] Reviews of Accelerator Science and Technology, Vol.2 and 4, A.W. Chao and W. Chou, World Scientific Publishing Co. Pte. Ltd. (2011)
- [2] T. Aaltonen et al. Phys. Rev. Lett. **109**, 071804, (2012)
- [3] Elizabeth Gibney and Davide Castelvecchi, Nature **626**, 468 (2024)
- [4] Strickland, D. and Mourou, G. Compression of amplified chirped optical pulses. Opt. Commun. **55**, 447–449 (1985)
- [5] T. Tajima and J. M. Dawson, Phys Rev Lett **43**, 267 (1979)
- [6] A. Modena et al., Nature (London) **377**, 606 (1995)
- [7] D. Umstadter et al., Science **273**, 472 (1996)
- [8] W. Leemans, B. Nagler, A. J. Gonsalves, Cs. Tóth, K. Nakamura, C. G. R. Geddes, E. Esarey, C. B. Schroeder and S. M. Hooker, Nature Physics **2**, 696 (2006)
- [9] S. Banerjee, N. D. Powers, V. Ramanathan, I. Ghebregziabher, K. J. Brown, C. M. Maharjan, S. Chen, A. Beck, E. Lefebvre, S. Y. Kalmykov, et al., PHYSICS OF PLASMAS **19**, 056703 (2012)
- [10] N. A. M. Hafz, Tae Moon Jeong, Il Woo Choi, Seong Ku Lee, Ki Hong Pae, Victor V. Kulagin, Jae Hee Sung, Tae Jun Yu, Kyung-Han Hong, Tomonao Hosokai, et al., Nature Photonics **2**, 571 (2008)
- [11] S. Kneip, S. R. Nagel, S. F. Martins, S. P. D. Mangles, C. Bellei, O. Chekhlov, R. J. Clarke, N. Delerue, E. J. Divall and G. Doucas, et al., PRL **103**, 035002 (2009)
- [12] X. Wang, Rafal Zgadzaj, Neil Fazel, Zhengyan Li, S. A. Yi, Xi Zhang, Watson Henderson, Y.-Y. Chang, R. Korzekwa, H.-E. Tsai, C.-H. Pai, et al., Nature Communiactions **4**, 1988 (2013)
- [13] M. Mirzaie, S. Li, M. Zeng, N. A. M. Hafz, M. Chen, G. Y. Li, Q. J. Zhu, H. Liao, T. Sokollik, F. Liu, Y. Y. Ma, et al., Scientific Reports **5**, 14659 (2015)
- [14] Jason M. Cole et al., PNAS **115**, 6335 (2018)
- [15] D. Storey et al., Phys. Rev. Accel. Beams **27**, 051302 (2024)
- [16] E. Esarey, C. B. Schroeder, and W. P. Leemans, Rev Mod Phys **81**, 1229 (2009)
- [17] Bernard Hidding, Andrew Beaton, Lewis Boulton, Sebastián Corde, Andreas Doepp, Fahim Ahmad Habib, Thomas Heinemann, Arie Irman, Stefan Karsch, Gavin Kirwan, Alexander Knetsch et al., Applied Science **9**, 2626 (2019)
- [18] R. S. Nagymihaly et al. Optics Express **31**, 44160 (2023)
- [19] Radier C, Chalus O, Charbonneau M, et al., 10 PW peak power femtosecond laser pulses at ELI-NP. High Power Laser Science and Engineering. **10**, e21 (2022)
- [20] W. Leemans, A. J. Gonsalves, H. S. Mao, K. Nakamura, C. Benedetti, C.B. Schroeder, Cs. Tóth, J. Daniels, D. E. Mittelberger, S. S. Bulanov, J.-L. Vay, C. G. R. Geddes, and E. Esarey, Phys. Rev. Lett. **113**, 245002 (2014)
- [21] A. J. Gonsalves, K. Nakamura, J. Daniels, C. Benedetti, C. Pieronek, T. C. H. de Raadt, S. Steinke, J. H. Bin, S. S. Bulanov, J. van Tilborg, C. G. R. Geddes, C. B. Schroeder, et al., Phys. Rev. Lett. **122**, 084801 (2019)

- [22] J. M. Cole et al., Phys. Rev. X **8**, 011020 (2018)
- [23] K. Poder et al., Phys Rev X **8**, 031004 (2018)
- [24] ILC <https://linearcollider.org/>
- [25] S. M. Mewes et al., Phys Rev Res **5**, 033112 (2023)
- [26] B. Miao, J. E. Shrock, L. Feder, R. C. Hollinger, J. Morrison, R. Nedbailo, A. Picksley, H. Song, S. Wang, J. J. Rocca, and H. M. Milchberg, Phys Rev X **12**, 031038 (2022)
- [27] Kosta Oubrerie, Adrien Leblanc, Olena Kononenko, Ronan Lahaye, Igor A. Andriyash, Julien Gautier, Jean-Philippe Goddet, Lorenzo Martelli, Amar Tafzi, Kim Ta Phuoc, Slava Smartsev and Cédric Thauy, Light: Science and Applications **11**, 180 (2022)
- [28] A. Picksley et al., Phys Rev E **102**, 053201 (2020)
- [29] A. Alejo et al., PRAB **25**, 011301 (2022)
- [30] E. Esarey, B. A. Shadwick, C. B. Schroeder and W. P. Leemans, AIP Conference Proceedings **737**, 578 (2004)
- [31] A. Debus, Richard Pausch, Axel Huebl, Klaus Steiniger, René Widera, Thomas E. Cowan, Ulrich Schramm, and Michael Bussmann, Phys Rev X **9**, 031044 (2019)
- [32] J. P. Palastro, J. L. Shaw, P. Franke, D. Ramsey, T. T. Simpson, and D. H. Froula, Phys Rev Lett **124**, 134802 (2020)
- [33] James D. Sadler, Christopher Arran, Hui Li, and Kirk A. Flippo, Phys. Rev. Accel. Beams **23**, 021303 (2020)
- [34] T. R. Clark and H. M. Milchberg, Phys Rev E **61**, 1954 (2000)
- [35] A. Picksley, et al., Phys Rev Lett **131**, 245001 (2023)
- [36] J. E. Shrock et al., Phys Rev Lett **X**, accepted (2024)
- [37] W. B. Mori, IEEE J. of Quantum Electronics, **33**, 1942 (1997)
- [38] J. R. Marques et al., Physics of Plasmas **5**, 1162 (1998)
- [39] P. Sprangle et al., Phys Rev A **36**, 2773 (1987)
- [40] V. F. Kovalev and V. Yu. Bychenkov, JETP Letters **107**, 458-463 (2018)
- [41] C. Benedetti et al., Phys Rev E **92**, 023109 (2015)
- [42] C. Benedetti et al., Phys. Plasmas **19**, 053101 (2012)
- [43] E. Esarey, P. Sprangle, J. Krall and A. Ting, Self-Focusing and Guiding of Short Laser Pulses in Ionizing Gases and Plasmas, IEEE JOURNAL OF QUANTUM ELECTRONICS, **33**, 1879 (1997)
- [44] D. F. Gordon et al., Phys. Rev. Lett. **90**, 215001 (2003)
- [45] J. Faure et al., Phys. Rev. Lett. **95**, 205003 (2005)
- [46] Zs. Léczi et al., Plasma Phys. Control. Fusion **65**, 105001 (2023)
- [47] A. Picksley, et al., Phys Rev Lett **133**, 255001 (2024)
- [48] S. Corde et al., Nature Comm **4**, 1501 (2013)

- [49] S. Shiraishi et al., *Physics of Plasmas* **20**, 063103 (2013)
- [50] W. Lu, M. Tzoufras, C. Joshi, F. S. Tsung, W. B. Mori, J. Vieira, R. A. Fonseca, and L. O. Silva, *Phys. Rev. ST Accel. Beams* **10**, 061301 (2007)
- [51] <https://www6.slac.stanford.edu/>; V. Balakin et al., *Phys Rev Lett* **74**, 2479 (1995)
- [52] R. Lehe, Manuel Kirchen, Igor A. Andriyash, Brendan B. Godfrey, Jean-Luc Vay, *Computer Physics Communications* **203**, 66-82 (2016)